Revealing Roles of Co and Ni in Mn-Rich Layered Cathodes

Weiyuan Huang, Cong Lin, Mingjian Zhang,* Shunning Li, Zhefeng Chen, Wenguang Zhao, Chen Zhu, Qi Zhao, Haibiao Chen, and Feng Pan*

Pressing demand for reducing the dependence of the costly Co and Ni elements has recently made Mn-rich layered oxides much more attractive as potential cathodes for rechargeable lithium-ion batteries. Although the Co and Ni effects in Ni-rich cathodes are investigated in detail, there is still a serious lack of fundamental understandings of the influences of the Co and Ni substitution on the structural and electrochemical properties of the Mn-rich layered cathodes. Here, Co-substituted, Co and Ni co-substituted, and Ni-substituted Mn-rich layered cathodes Li(Mn, Ni, Co)O2 are consciously designed to explore the roles of Co and Ni. These results elucidate that Co⁴⁺ is destructive for the structural stability of Mn-rich cathodes due to the increased instability in the lattice oxygen, especially at high potentials, thereby delivering poor cycling stability, while Ni substitution of Co introduces Li/Ni mixing to enhance the lattice oxygen stability and suppress phase segregation and irreversible phase transition, leading to much improved cycling stability. These findings complement the elemental chemistry of the Co-, Ni-, and Mn-based layered oxide cathodes, and benefit the development of Co-free Mn-rich layered cathode materials for future rechargeable lithium-ion batteries.

1. Introduction

Rechargeable lithium-ion batteries (LIBs) have undoubtedly innovated today's portable electronics and electrical vehicles. However, the performance of the state-of-the-art LIBs is still limited by that of the cathode, which is normally the largest component in terms of both the weight and cost.^[1,2] Therefore, developing the cathodes possessing both the high performance and low cost has been one of the frontiers in the LIB field. Although the Co-containing cathodes like LiCoO₂ (LCO),^[3,4] ternary Li(Ni_xMn_yCo₂)O₂ (NMC; x + y + z = 1; x > 1/3), [5,6] and $\text{Li}(\text{Ni}_{0.80}\text{Co}_{0.15}\text{Al}_{0.05})\text{O}_2$ (NCA) $^{[7,8]}$ are now widely used in the current commercial batteries, the call for low-Co and Co-free cathodes is an unstoppable trend due to the high cost, high

W. Huang, C. Lin, M. Zhang, S. Li, Z. Chen, W. Zhao, C. Zhu, Q. Zhao, School of Advanced Materials

Peking University Shenzhen Graduate School

Shenzhen 518055, P. R. China

E-mail: zhangmj@pkusz.edu.cn; panfeng@pkusz.edu.cn

H. Chen

Institute of Marine Biomedicine Shenzhen Polytechnic

Shenzhen 518055, P. R. China



The ORCID identification number(s) for the author(s) of this article can be found under https://doi.org/10.1002/aenm.202102646.

DOI: 10.1002/aenm.202102646

toxicity, and child labor abuse in mining of Co.[9-13,15] In contrast, the price of Ni is only one-third of Co, whereas Mn is even cheaper at a fifth of the price of Ni, while the global Mn reserves are even two orders of magnitude higher than those of Ni and Co (Figure S1, Supporting Information).^[2,14–16] Furthermore, the biological toxicity of Mn is also much less than that of Co and Ni. Therefore, the Mn-rich cathodes are highly competitive both economically and environmentally due to the significantly lower price from the much larger reserves as well as the safety considerations. Several candidates, including two spinel Mn-rich oxides LiMn₂O₄ and LiNi_{0.5}Mn_{1.5}O₄, have been mentioned as the potential alternatives to the Cocontaining cathodes.[17-20] However, the relatively low capacity and energy density of these new options hinder their commercial success in electric vehicles.

Mn-rich layered oxide possesses a capacity comparable with the current commercial LCO and Ni-rich NMC and NCA cathodes, and has become a research hotspot as the promising LIB cathode. [21,22] As the qualitative comparison regarding the performance between the Mn-rich layered oxide and other representative LIB cathodes shown in Figure S2 (Supporting Information), it is obvious that the advantages of this kind of material in terms of both the low cost and the high capacity are much prominent. Typical Mn-rich layered oxide is the nonstoichiometric Li-excess Li(Li_{1/3}Mn_{2/3})O₂ (or Li₂MnO₃), whose electrochemical activation process unfortunately imposes serious limitations on the cathode performance with poor cyclic capacity, rapid voltage decay, and structural damage. [23-26] The other Mn-rich layered oxide type is the stoichiometric LiMnO2; however, studies have already proved it to be inappropriate for practical applications due to the irreversible phase transition from layered to spinel phase during cycling, which causes severe capacity degradation. [27-29] Fortunately, partial substitution of Mn by Co or Ni (LiMn₁ $-_x$ M_xO₂, M = Co, Ni; 0 < x ≤ 0.5) has been confirmed to be a feasible route to enhance the electrochemical performance of the Mn-rich layered cathodes, [30,31] which possess the similar layered structure with the NMC cathodes (Figure 1a). In the ternary NMC system, although the Ni-rich layered oxides have extensively been studied (green spots in Figure 1b), like the typical NMC811, NMC71515, and NMC622,[32-36] the Mnrich layered oxide system is still unexploited to a great extent. Specifically, the layered cathodes have rarely been reported

16146480, 2021, 41, Downloaded from https://dwnneed.onlinelibrary.wiely.com/oi/01002/aen.20/2102646 by University Town Of Sheraben, Wiley Online Library on [2411025], See he Terms and Conditions (https://onlinelibrary.wiely.com/terms-and-conditions) on Wiley Online Library for rules of use; OA articles are governed by the applicable Cerative Commons

www.advancedsciencenews.com www.advenergymat.de

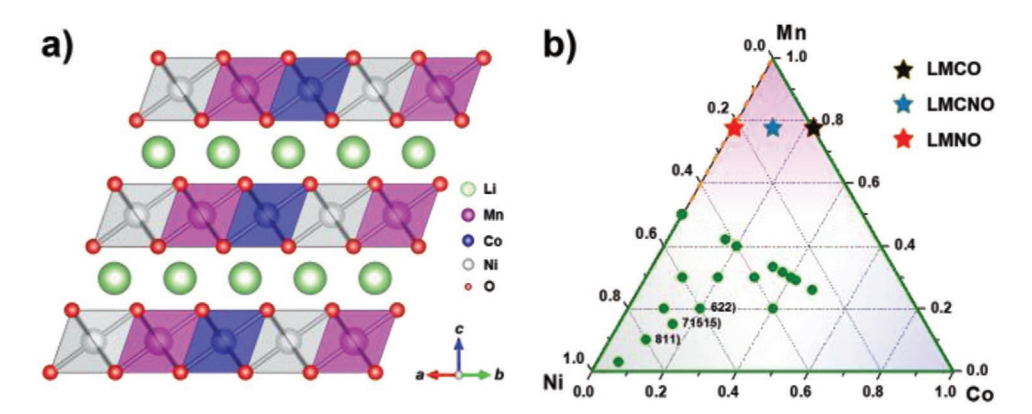


Figure 1. Structure and phase diagram of the NMC ternary layered cathodes. a) Schematic illustration for the crystal structure of the NMC ternary layered oxide cathode. b) Ni–Co–Mn ternary elemental phase diagram showing the reported NMC layered oxide cathodes in green. Three Mn-rich layered oxides in this work are marked by the pentagrams.

to possess the Mn content larger than that of the Li-excess $\text{Li}(\text{Li}_{1/3}\text{Mn}_{2/3})\text{O}_2$, in addition to the few reports on the Mn–Ni and Mn–Co binary Mn-rich layered oxides with the maximum Mn content as $0.5.^{[37-40]}$

Thoroughly understanding the individual elemental roles has always been at the most forefront for the battery material development. Co, Ni, and Mn are the most primary components in the layered cathodes but their specific roles in various materials may differ a lot. To be specific, the roles of the Ni and Mn substitution in the LiCoO2 cathode have been demonstrated as improving the structural and electrochemical stability by suppressing the adverse phase transitions. [41,42] while some studies also attribute the Ni function to the Li/Ni mixing effect.^[43] For the Ni-rich layered cathodes, the Mn and Co roles have also been extensively investigated. Specifically, Mn has widely been accepted to enhance the structural stability,[14] but the role of Co has two sides. On the one hand, Co can enhance the electronic conductivity and suppress the Li/Ni mixing in the Ni-rich layered cathodes,[44-46] thereby increasing the rate capability and the specific capacity. On the other hand, recent studies have revealed that at high potentials, Co, rather than Ni, is more destructive to the structural stability due to the overlap of the density states between the O 2p and $\text{Co}^{3+/4+}$ t_{2g} , which overpromotes the lattice oxygen activity and may even be considered to be removed from the Ni-rich NMC series. [15,47] In addition, another notable phenomenon in the Ni-rich layered oxides is the Li/Ni mixing. The antisite Ni2+ cations in the Li layers impede the Li+ extraction/insertion and damage the capacity,[48-50] while they can also act as pillars of the Li layers to mitigate the structure collapse at the high charge state.^[51] Nevertheless, despite that the Co and Ni roles in the Li- and Mn-rich layered cathodes have been previously studied, with the functions like Co promoting the capacity but deteriorating the stability at high potentials and Ni suppressing the capacity and voltage fading through the Li/Ni mixing, [52,53] the exact impacts of Co and Ni on the structural stability as well as the electrochemical performance of the Mn-rich layered oxide cathodes with a much higher Mn content still remain unclear.

Herein, three typical Mn-rich layered oxides, $\text{Li}_{0.7}\text{Mn}_{0.78}\text{Co}_{0.22}\text{O}_2$ (LMCO), $\text{Li}_{0.75}\text{Mn}_{0.78}\text{Co}_{0.11}\text{Ni}_{0.11}\text{O}_2$ (LMCNO), and $\text{Li}_{0.74}\text{Mn}_{0.78}\text{Ni}_{0.22}\text{O}_2$ (LMNO), are purposely designed with

an unexploited high Mn content (i.e., 0.78) to investigate the impacts of the Co and Ni substitution on the structural stability and electrochemical performance of the Mn-rich cathodes (marked by the pentagrams in Figure 1b). Comparative structural analyses and electrochemical measurements reveal that the Co-substituted LMCO shows overhigh lattice oxygen activity and suffers from severe oxygen loss and phase segregation at the high charge state, resulting in the irreversible phase transition to spinel phase and lots of microcracks in the primary particles during cycling. In contrast, Ni introduction of LMCNO and LMNO leads to the interlayer Li/Ni mixing and the unique local oxygen configurations of TM₂Li-O-NiLi₂ (TM: transition metals) and TM₃-O-NiLi₂, which can efficiently suppress the lattice oxygen loss and the phase segregation at high potentials and enhance the structural stability of the anionic framework, thus resulting in the superior electrochemical performance. Our work not only represents an important addition to the elemental chemistry of the Co-, Ni-, and Mn-based layered cathodes but also highlights the potential for achieving the Co-free Mn-rich layered cathodes with high energy density for future commercial rechargeable LIB applications.

2. Results and Discussion

2.1. Impacts of Co and Ni Substitution on Layered Structure

Three lithium Mn-rich layered oxides, LMCO, LMCNO, and LMNO, were prepared by the ion exchange process with the corresponding sodium-containing Mn-rich layered oxide precursors NMCO, NMCNO, and NMNO. Figure 2a presents the X-ray diffraction (XRD) patterns of three precursors, all of which can be well assigned to the P2-type layered structure (left panel of Figure 2g) without obvious impurity. After ion exchange, the particle size and morphology of the three products were first characterized by scanning electron microscopy (SEM), showing the sphere-like secondary particles with a diameter of 1–2 μ m (Figure S3a–c, Supporting Information), while energy dispersive spectroscopy (EDS) suggests the uniform distribution of Mn, Co, and Ni in the grains (Figure S3d–f, Supporting Information). The chemical formulae were later identified by the

16146840, 2021, 41, Downloaded from https://advanced.onlinelibrary.wiley.com/doi/10.1002/aenm.202102646 by University Town Of Shenzhen, Wiley Online Library on [24/11/2025]. See the Terms

and Conditions (https://onli

and-conditions) on Wiley Online Library for rules of use; OA articles are governed by the applicable Creative Commons

www.advancedsciencenews.com

www.advenergymat.de

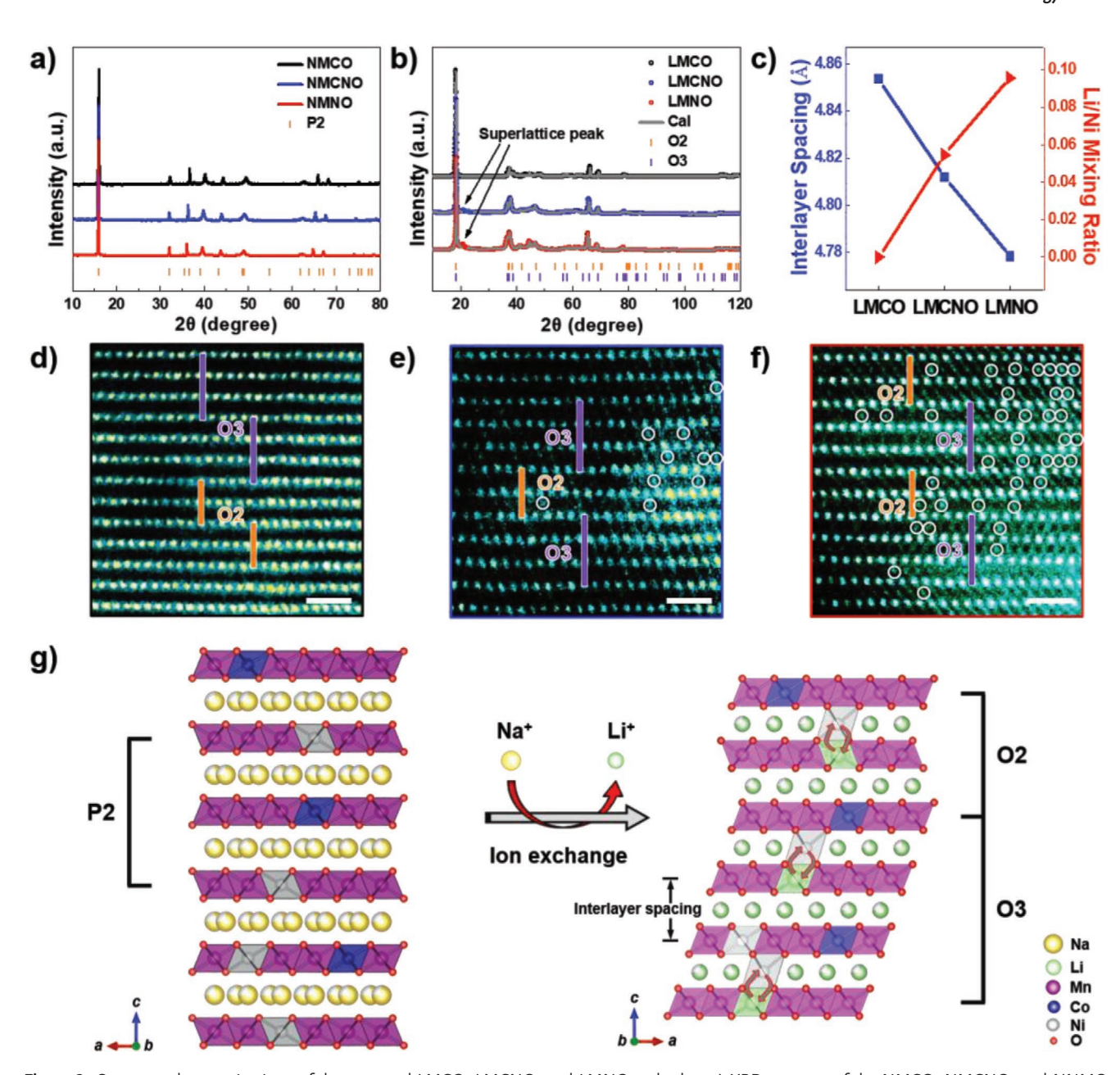


Figure 2. Structure characterizations of the prepared LMCO, LMCNO, and LMNO cathodes. a) XRD patterns of the NMCO, NMCNO, and NNMO precursors. b) Rietveld refinement against the XRD patterns of LMCO, LMCNO, and LMNO. c) Variation of the interlayer spacing and Li/Ni mixing ratio when Co is substituted by Ni. d–f) HAADF-STEM images of LMCO, LMCNO, and LMNO, respectively, with the antisite Ni highlighted by the white circle (scale bar: 1 nm). g) Schematic of the Na⁺/Li⁺ ion exchange process from the P2-type layered Na-containing precursor to the complex layered Li-containing products. The double arrows are used to represent the Li/Ni mixing.

inductively coupled plasma-optical emission spectroscopy (ICPOES) as $\mathrm{Li_{0.75}Mn_{0.78}Co_{0.22}O_2}$ for LMCO, $\mathrm{Li_{0.75}Mn_{0.78}Co_{0.11}Ni_{0.11}O_2}$ for LMCNO, and $\mathrm{Li_{0.74}Mn_{0.78}Ni_{0.22}O_2}$ for LMNO (Table S1, Supporting Information), confirming not only the Mn-rich and the Li-deficient characters but also the complete $\mathrm{Li^+/Na^+}$ ion exchange. The differential scanning calorimetry (DSC) measurement was carried out to evaluate the thermal stability of the three oxides, showing the onset of the exotherm (heat release) commencing at 158, 161, and 167 °C for LMCO, LMCNO, and LMNO, respectively (Figure S4, Supporting Information). This suggests that the Ni substitution can improve the thermal

stability of the Mn-rich layered oxides to some extent. XRD patterns of LMCO, LMCNO, and LMNO, and Rietveld refinements were conducted to check their structures (Figure 2b; Table S2, Supporting Information). It is interesting to see that two layered phases O3 and O2 co-exist for three samples in a similar phase ratio of 0.85:0.15. Thereinto, the O2 phase directly derives from the P2-type precursor while the O3 phase may be induced by the excessive Li⁺ insertion. More importantly, some differences in XRD patterns can be observed to analyze the different impacts of Co and Ni substitution on the layered structures. First, the peak intensity at high angles is

www.advenergymat.de

16146849, 2021, 41, Downloaded from https://advanced onlinelibrary.wiely.com/doi/10.1002/aem.m.202102646 by University Town Of Shenzhen, Wiley Online Library on [2411.0225]. See the Terms and Conditions (https://onlinelibrary.wiely.com/terms-and-conditions) on Wiley Online Library for rules of use; OA archies are governed by the applicable Centwise Commons I

evidently increased with a narrower peak shape from LMCO to LMCNO then to LMNO, implying that Ni benefits improving the crystallinity of the layered oxides (Figure S5, Supporting Information). Another difference is that a superlattice peak emerges at ≈20.8° for the Ni-substituted samples (marked by the arrows in Figure 2b), while absent in LMCO. It can be assigned to the LiTM6 superlattice ordering in the TM layers of the layered phases, i.e., one LiO6 octahedron surrounded by six TMO6 octahedra, which was reported extensively in Lirich layered cathodes but observed here in Li-deficient layered oxides for the first time. Moreover, the normalized intensity of the superlattice peak increases from Co-contained LMCNO to Co-free LMNO, further confirming that Ni can induce the formation of LiTM6 ordering in TM layers, while Co just leads to the Co/Mn disordering in TM layers. In addition, Li/Ni mixing and the interlayer spacing (Figure 2g) are extracted from Rietveld refinements (Figure 2c). It is clear that more Ni substitution would encourage Li/Ni mixing and decrease the interlayer spacing in layered phases, while Co plays the inverse role. The above phenomenon observed in Mn-rich layered oxides is consistent with that revealed in Ni-rich layered oxides^[49,54] and can be interpreted by the superexchange interactions.^[48]

The layered structures of the three samples are further confirmed by the high-resolution transmission electron microscopy (HRTEM) images as well as the corresponding fast Fourier transform (FFT) patterns (Figure S3g-i, Supporting Information). To check the local structural details, atomicresolution high-angle annular dark-field scanning transmission electron microscopy (HAADF-STEM) images were performed (Figure 2d-f). It is clear that mixed O3 and O2 arrangements of the TM atoms are directly observed (marked by the purple and orange lines, respectively), which are consistent with the phase analysis based on XRD patterns above. It also reflects that two phases are well integrated along the direction perpendicular to the TM layers at the scales of one-unit-cell thickness. Moreover, empty Li layers by bright contrast indicate that no antisite TM cations are observed in the HADDF-STEM image of LMCO. In comparison, lots of bright spots are observed in Li layers of LMCNO and LMNO, indicating serious Li/Ni mixing with the increase of Ni content, in accordance with the XRD results.

In brief, Ni substitution can simultaneously enhance the intralayer cationic ordering with LiTM6 superstructure units but decreases the interlayer cationic ordering by promoting Li/Ni mixing, in contrast to Co substitution. This is different from previous studies that mainly focus on the Ni content and Li/Ni mixing as well as their influences on the electrochemical properties. [51,55,56]

2.2. Impacts of Co and Ni Substitution on Electrochemistry

The electrochemical performances of the three materials were evaluated to check the impacts of Co and Ni. **Figure 3**a presents the capacity profiles of LMCO, LMCNO, and LMNO cathodes in the voltage range of 2.0–4.8 V at 0.1C (1C = 200 mA g⁻¹), giving the discharge capacity in the first cycle of 263, 245, and 235 mA h g⁻¹, respectively. The rate performance is shown in Figure 3b. Despite the slightly smaller capacity of LMCNO and LMNO than LMCO, Ni substitution can evidently improve

the rate performance to some extent, especially at high rates. This also corresponds to the much smaller impedance increase in LMNO for the first several cycles, as shown in the electrochemical impedance spectroscopy (EIS; Figure S6, Supporting Information). Detailed Li-ion diffusion coefficients for LMCO, LMCNO, and LMNO after the initial three cycles were determined via the galvanostatic intermittent titration technique (GITT; Figure S7a-c, Supporting Information). As displayed in Figure S7d (Supporting Information), the calculated Li-ion diffusion coefficients in the discharge process are at the same order of magnitude of 10⁻¹³ cm² s⁻¹ at the initial stage, and go down to 1.3×10^{-15} , 2.4×10^{-15} , and 1.35×10^{-14} cm² s⁻¹ at the final stage for LMCO, LMCNO, and LMNO, respectively. It indicates the faster Li-ion diffusion kinetics in the Ni-substituted materials, in consistence with the superior rate performance. The cyclic voltammetry (CV) curves for the first three cycles are plotted in Figure S8 (Supporting Information). With Ni substitution, the CV peaks become much sharper. More importantly, the peak at >4.5 V in the first charge process is notably attenuated, which can be ascribed to the weakening of the anionic redox reaction, in accordance with the shorter plateau in the first charge curve with the Ni substitution (Figure 3a). And the CV peaks at ≈ 3.0 , > 3.6, and > 4.0 V are attributed, respectively, to the redox pairs of Mn³⁺/Mn⁴⁺, Co³⁺/Co⁴⁺, andNi²⁺/Ni⁴⁺. To evaluate the effect of Li deficiency, the capacity profiles of the first cycle after the prelithiation treatment are also characterized and presented in Figure S9 (Supporting Information). They deliver a similar capacity at around 250 mA h g⁻¹, and the Ni-substituted LMCNO and Co-free LMNO exhibit higher Coulombic efficiency (CE) than LMCO (86.8%, 91.1%, and 92.2% for LMCO, LMCNO, and LMNO, respectively), indicating a higher energy conversion efficiency with Ni substitution. To further investigate their cyclic capacity and voltage stability, long-cycle tests were conducted at 0.25C, and the corresponding results are shown in Figure 3c,d. Although LMCO exhibited both higher initial capacity and average voltage, unfortunately, its capacity retention was only 53% and the voltage decay reached ≈0.38 V after 100 cycles. In a sharp contrast, LMNO demonstrated the best capacity retention of 88% and the lowest voltage decay of ≈0.11 V. The similar trend can also be found in a narrower voltage region of 2.0-4.5 V (Figure S10, Supporting Information).

The discharge profiles of LMCO, LMCNO, and LMNO at the specific 2nd, 10th, 20th, 50th, and 100th cycles with the corresponding dQ/dV curves are shown in Figure S11 (Supporting Information) to preliminarily clarify their degradation behavior upon cycling. An obvious shift to the lower voltage region of the redox peaks at \approx 2.8 and >4.0 V was observed in LMCO. Such a shift tendency was suppressed to some degree in the Ni-substituted LMCNO and LMNO, also indicating the more stable electrochemical performance by Ni substitution.

For a more in-depth study of the Ni and Co roles on the electrochemical performance of the Mn-rich layered oxides, different contents of Ni and Co substitution were also taken into account, and the electrochemical performances cycled in the voltage range of 2.0–4.8 V at 0.25 C are shown in Figure S12 (Supporting Information). Specifically, as the Ni substitution content increases from 15% (LMNO-15%) to 22% (LMNO), 35% (LMNO-35%), and 45% (LMNO-45%), the corresponding

16146840, 2021, 41, Downloaded from https://advancec

onlinelibrary.wiley.com/doi/10.1002/aenm.202102646 by University Town Of Shenzhen, Wiley Online Library on [24/11/2025]. See the Terms

and Conditions (https://onlinelibrary.wiley.com/term

and-conditions) on Wiley Online Library for rules of use; OA articles are governed by the applicable Creative Commons

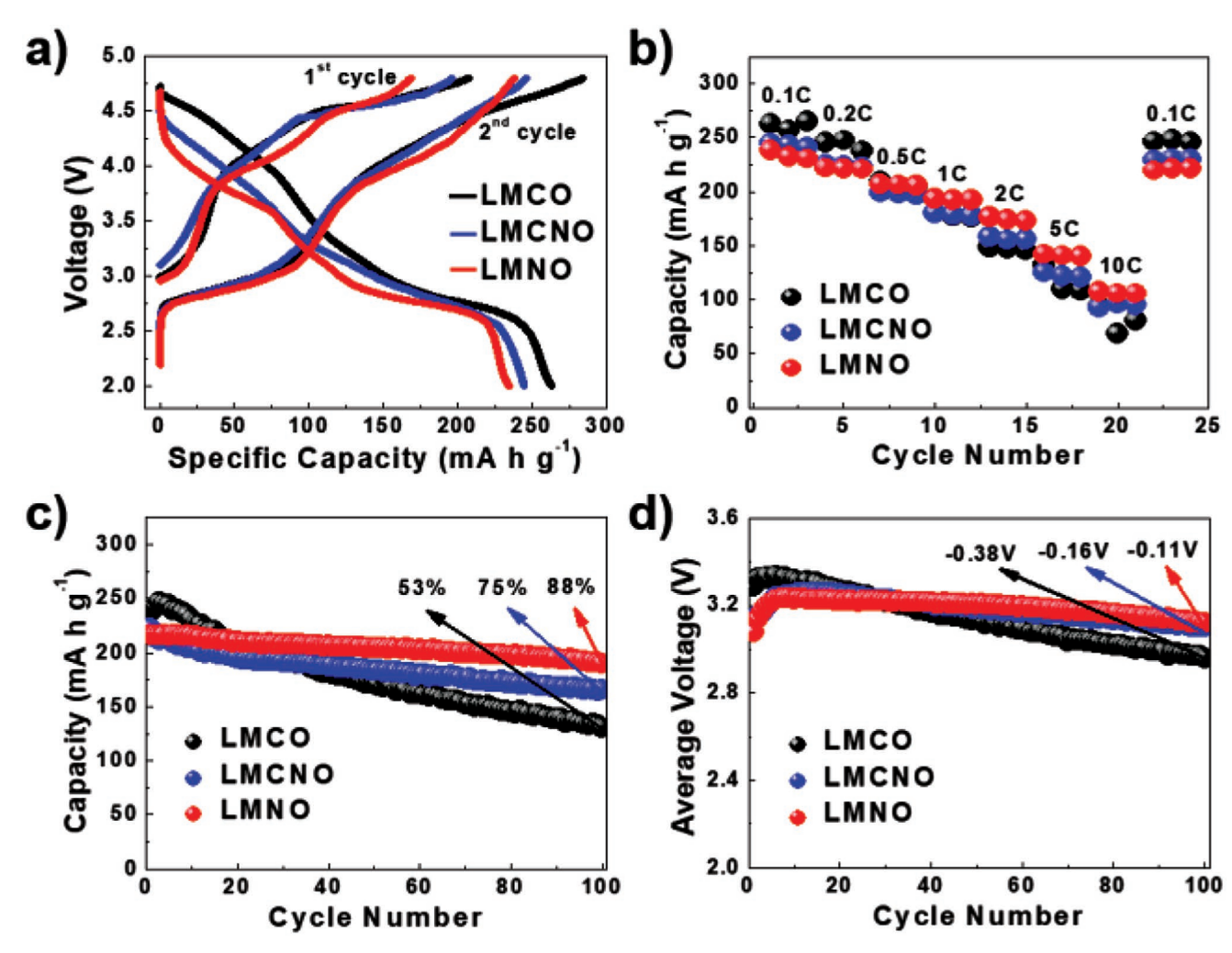


Figure 3. Electrochemical performances of the LMCO, LMCNO, and LMNO cathodes. a) Charge/discharge curves in the voltage range of 2.0–4.8 V at 0.1C rate. b) Rate performance. c) Capacity stability. d) Average voltage stability at 0.25C rate.

first discharge capacity decreases from 223 to 216, 185, and 141 mA h g⁻¹, but the capacity retention after 100 cycles raises from 82% to 88%, 91%, and 94%, respectively (Figure S12a, Supporting Information). In a sharp contrast, when the Co substitution content increases similarly from 15% (LMCO-15%) to 22% (LMCO), 35% (LMCO-35%), and 45% (LMCO-45%), the corresponding capacity retention decreases rapidly from 81% to 76%, 75%, and 73% after only 35 cycles, despite the higher initial discharge capacity than that of the Ni-substituted counterparts (Figure S12b, Supporting Information). It can thus be clearly concluded from the above results that when the Mn-rich layered cathode is cycled upon the upper cutoff voltage of 4.8 V, the Co substituion is destructive for the structural stability, while Ni is beneficial for stabilizing the structure but a high Ni substitution content results in the sacrificed practical capacity.

2.3. Structural Stability during Charge/Discharge

The electrochemical performance of battery materials is known to be greatly determined by the intrinsic structures. Thus, ex

situ XRD measurement was carried out to investigate the structural changes of the three cathode materials during the first electrochemical cycle (Figure S13a-c, Supporting Information). The main peaks in the region of 17°-20.5° are enlarged to check the subtle structural changes (Figure 4a-c). For LMCO, the diffraction peak at ≈18.25° slightly shifts to higher angle during the charge process from the open-circuit voltage (OCV) to 4.3, 4.5, and 4.8 V, indicating the shrinkage of the interlayer spacing (indicated by the arrow in Figure 4a). Besides, a new peak appears at ≈19.23° when charged to 4.8 V, suggesting the phase segregation of LMCO at high voltages, which leads to a serious lattice mismatch as indicated by the large difference of the interlayer spacing ($\Delta d = 0.21 \text{ Å}$). A similar phenomenon was observed in the deep delithiated LiCoO2 due to the transition to the H1-3 phase. [3,4] When discharged to 2 V, the two peaks merge to one with broadened shape and a shoulder peak, but never fully returned to the original position. Such serious phase segregation and big lattice mismatch in LMCO at high potentials would accumulate tremendous stress at the phase boundaries and further induce lots of microcracks within primary particles, as directly observed in Figure 4d and in Figure S14a,b

www.advenergymat.de

16146840, 2021, 41, Downloaded from https://advanced.onlinelibrary.wiley.com/doi/10.1002/enm.202102646 by University Town Of Shenzhen, Wiley Online Library on [24/11/2025]. See the Terms and Conditions (https://onlinelibrary.wiley

and-conditions) on Wiley Online Library for rules of use; OA articles are governed by the applicable Creative Commons

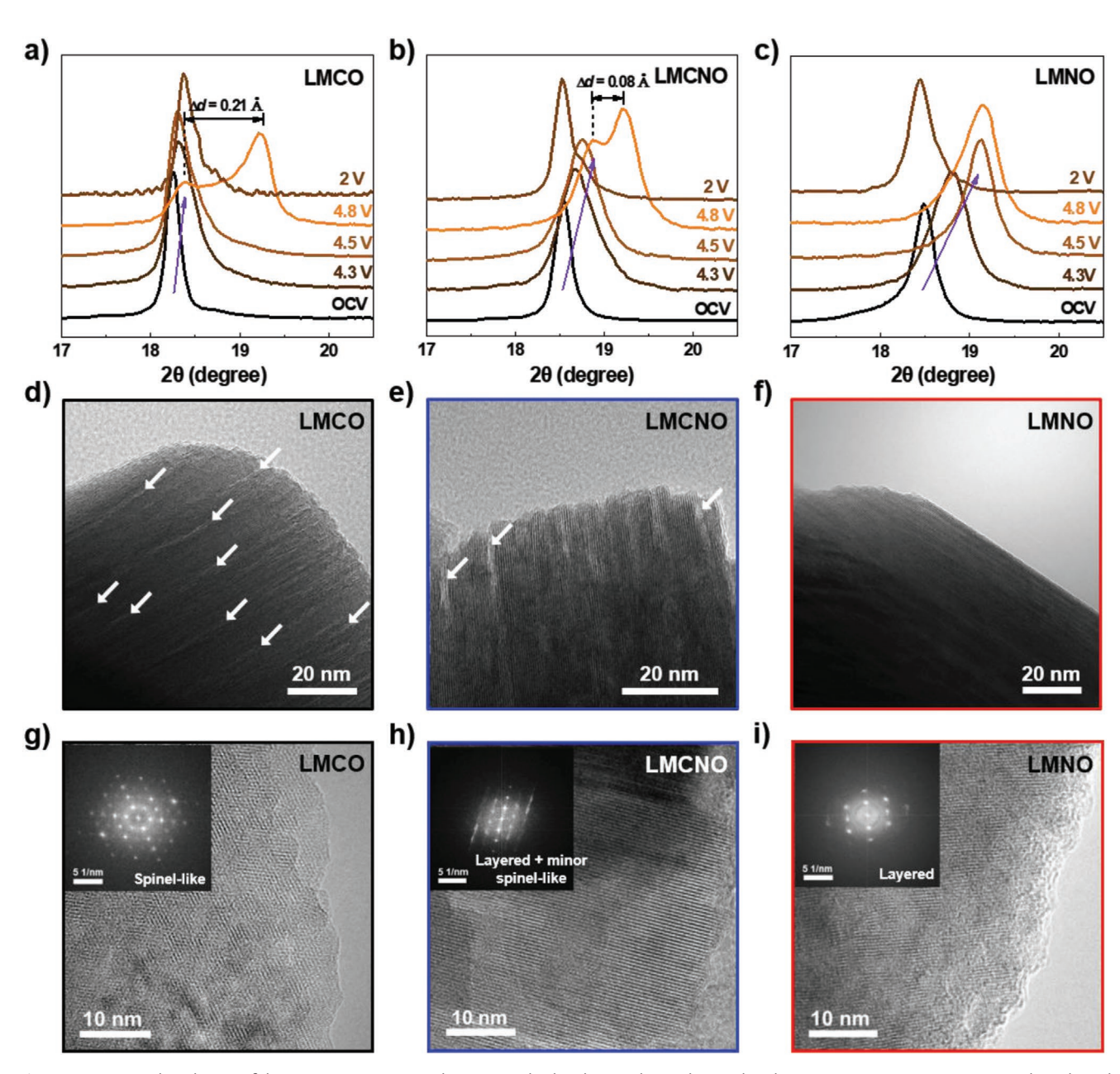


Figure 4. Structural evolution of the LMCO, LMCNO, and LMNO cathodes during electrochemical cycling. a–c) Ex situ XRD patterns at the selected charge/discharge states during the first electrochemical cycle. The complete patterns are presented in Figure S13 (Supporting Information). d–f) HRTEM images after the first charge to 4.8 V with the microcracks highlighted by the white arrows. g–i) HRTEM images with corresponding FFT patterns after 100 cycles.

(Supporting Information). As for LMCNO, the main peak shifts to the same direction as LMCO, but, to a greater extent, with charging. Phase segregation also occurred for LMCNO at 4.8 V, as indicated by the peak splitting (Figure 4b). As compared with LMCO, the smaller difference between the interlayer spacings ($\Delta d = 0.08$ Å) means a smaller lattice mismatch. Therefore, the stress induced by phase segregation is believed to be alleviated in LMCNO, which is also confirmed by the fewer microcracks from the HRTEM image (Figure 4e; Figure S14d,e, Supporting Information). When discharged to 2.0 V, the two peaks also merge and shift to the initial position but with a small shoulder peak. On further increasing Ni content, the main peak for

LMNO shows a smooth shift from $\approx 18.50^{\circ}$ to 19.16° , and no visible peak splitting is observed even at 4.8 V, implying the absence of the phase segregation (Figure 4c). In addition, this peak can shift back to its original position when discharged to 2.0 V, demonstrating the good reversibility of the structural change. These results distinctly indicate that LMNO possesses a more stable structure during cycling, resulting in much less intragrain stress and microcracks, as demonstrated in Figure 4f and in Figure S14g,h (Supporting Information). Detailed microstructural analyses from the HRTEM images with the corresponding FFT patterns further suggest that the ≈ 15 nm thick surface region of the LMCO particle has transformed from

www.advenergymat.de

16146840, 2021, 41, Downloaded from https://advanced.onlinelibrary.wiley.com/doi/10.1002/aenm.202102646 by University Town Of Shenzhen, Wiley Online Library on [241112025]. See the Terms and Conditions (https://onlinelibrary.wiley.com/terms-and-conditions) on Wiley Online Library for rules of use; OA aricks are govered by the applicable Centwice Commons

the layered phase to the polycrystalline spinel-like phase after charging to 4.8 V (Figure S14c, Supporting Information), indicating the TM migration to the Li layers at high charge voltages. A similar spinel shell was observed on the particle surface of LMCNO but presents a feature of single crystal with a thinner thickness of 5 nm (Figure S14f, Supporting Information). In a sharp contrast, LMNO still maintained the layered structure both in the bulk and at the surface (Figure S14i, Supporting Information). These observations clearly validate that the structural stability of the Mn-rich layered cathodes can be greatly improved by the Ni substitution, which is responsible for the excellent cycling stability.

LMCO, LMCNO, and LMNO cathodes after 100 cycles were further characterized to illustrate their cyclic stability. Figure S15 (Supporting Information) shows the SEM images of the three resultant samples. One could identify that the LMCO particles possess obvious cracks and are covered with thick side-reaction species from reacting with the electrolyte, whereas LMCNO and LMNO still keep the original spherical secondary particle morphology with a relatively clean surface. Microstructural analyses were performed by HRTEM images with their corresponding FFT patterns shown in Figure 4g-i and in Figure S16 (Supporting Information). A thick region from the particle surface of LMCO has nearly transformed to the spinel-like phase with high crystallinity (Figure 4g; Figure S16a-c, Supporting Information), indicating that the irreversible transition from the layered to spinel-like phase occurs from the particle surface to the interior. The irreversible transition is partially suppressed as indicated by the weak spinel-like signal from the FFT pattern in LMCNO (Figure 4h; Figure S16d-f) and the absence of spinel signal in LMNO (Figure 4i; Figure S16g-i, Supporting Information). These are in accordance with the XRD and HRTEM results after the first charge to 4.8 V (Figure 4a-f; Figure S14, Supporting Information) and clearly prove again the more stable structure of LMNO.

To investigate the chemistry of the electrode-electrolyte interphases, the X-ray photoelectron spectroscopy (XPS) patterns with different etch depths of the cycled electrodes were collected and are shown in Figures S17 and S18 (Supporting Information). In the C 1s spectra (Figure S17a, Supporting Information), the peak located at 284.6 eV can be assigned to the C-C of the conductive carbon, while the peaks at 286 and 290.3 eV are the C-F signals from the polyvinylidene difluoride (PVDF) binder. The C-O peak at 286.6 eV and the C=O peak at 289 eV correspond to the polycarbonate or ROCO2Li species, which also correlate the peaks located at 531.5 eV (C=O) and 533.4 eV (C-O) in the O 1s spectra (Figure S17b, Supporting Information). Compared with LMCO showing negligible changes in the O 1s spectra, LMCNO and LMNO exhibit obvious intensity decrease in the C=O peak (531.5 eV) and intensity increase in the TM-O peak (529.5 eV) following the etch depth from 0 to 10 and 20 nm, which clearly indicates a much thinner cathodeelectrolyte interphase (CEI) film. In addition, the observed Li₂O deposited species located at 528.3 eV on the LMCO electrode surface can be related to the dissolution of transition metal.^[57] As for the F 1s spectra (Figure S17c, Supporting Information), the increased peak intensity with deeper etch depth at 685 eV for LMCO corresponds to the LiF formation inside the CEI film, while LMCNO and LMNO both show the decreased peak intensity as the etch depth reaches 20 nm, also implying the thinner CEI film than LMCO. As for the XPS results of the TM 2p (Figure S18, Supporting Information), the weak peak intensities of Mn 2p and Co 2p of LMCO reveal the thick deposited products on the electrode surface again, while LMCNO and LMNO show obviously strong peaks as the etch depth increases to 10 nm and 20 nm. These XPS results strongly confirm a much active interfacial decomposition reaction in the LMCO cathode, which may attribute to the overlap of the density of states between the O 2p and Co $^{3+/4+}$ t_{2g} and cause the formation of a thicker CEI film, [45,58] in agreement with the SEM images shown in Figure S15 (Supporting Information). Since the CEI is environmentally sensitive (air, water, etc.) and vulnerable to be damaged during the TEM sample preparation and by the high-energy electron beam as well, it cannot be easily observed in our TEM measurement.

Finally, the EIS was also conducted to investigate the cell impedance after the long-term cycling. As shown in Figure S19 (Supporting Information), the cathode impedance values for the LMCO, LMCNO, and LMNO half cells after 100 cycles are determined to be \approx 99, 50, and 48 Ω , respectively. This suggests a lower interfacial resistance and superior charge-transfer kinetics in the Ni-substituted LMCNO and the Co-free LMNO cathodes, [59,60] which is consistent with the above results from the SEM and HRTEM.

Based on the above measurements, it is thus reasonable to speculate that the substitution of Ni rather than Co has greatly improved the structural stability of the layered Mn-rich oxides during the long-term electrochemical cycling, leading to less phase separation and irreversible structural transition as well as reduced side reactions.

2.4. Lattice Oxygen Stability at Deep Charge State

To further explore the origin of the superior stability induced by Ni substitution, in situ differential electrochemical mass spectrometry (DEMS) was then employed as a probe for the interfacial side reactions and the lattice oxygen stability of the three cathodes. The results are shown explicitly in Figure 5a-c. During the charge process of LMCO (Figure 5a), O2 release starts when charged above 4.6 V, and proceeds until discharged to 4.6 V, reflecting the instability of the lattice oxygen. With Ni substitution, O2 release is undetectable, indicating that the stability of the lattice oxygen has been greatly improved (Figure 5b,c). In addition, two peaks for CO₂ release are observed for LMCO: one is located at ≈4.7 V during charge, and the other is recorded at ≈4.5 V during discharge, hinting at the serious surficial side reactions with the electrolyte. [10] As an apparent contrast, CO₂ release was greatly reduced for LMCNO (Figure 5b), while only a very weak CO₂ signal could be detected in the charge process of the Co-free LMNO (Figure 5c). These results also exhibit that Co would result in serious surficial side reactions, while Ni can suppress it to a great extent.

To explore the cause of the O_2 release, theoretical calculations were performed based on the O coordination configurations in LMCO and LMNO (Figure 5d,e). In LMCO, one O atom is coordinated with three TM and three Li atoms ($Mn_2Co-O-Li_3$; top panel in Figure 5f), while in LMNO, there

www.advenergymat.de

16146840, 2021, 41, Downloaded from https://advanced.onlinelibrary.wiley.com/doi/10.1002/aemm.202102646 by University Town Of Shenzhen, Wiley Online Library on [24/11/2025]. See the Terms and Conditions (https://onlinelibrary.wiley.com/terms-

and-conditions) on Wiley Online Library for rules of use; OA articles are governed by the applicable Creative Commons

www.advancedsciencenews.com

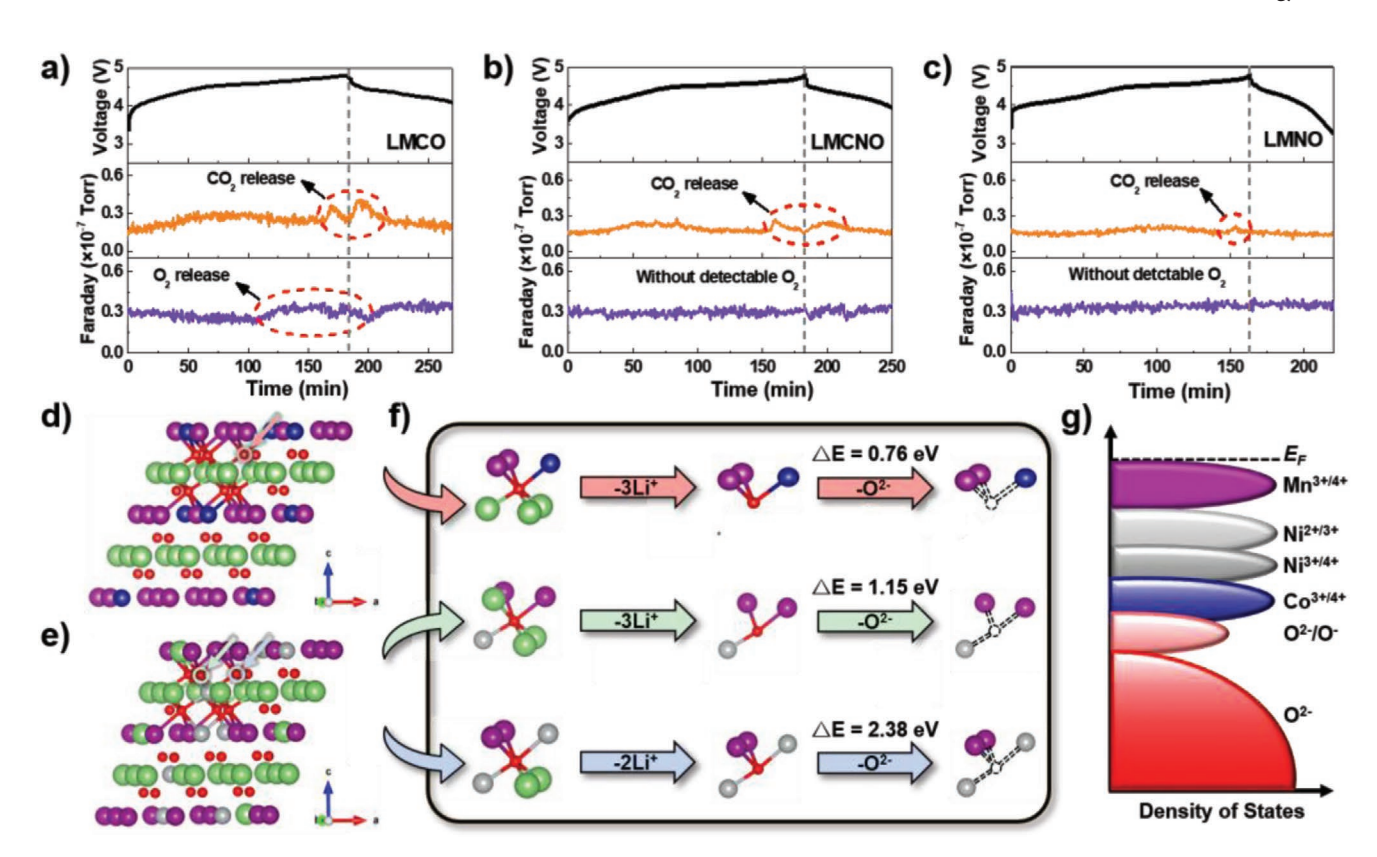


Figure 5. Origin of the improved O stability by Ni substitution. a–c) In situ DEMS results of LMCO, LMCNO, and LMNO during the first cycle. The gas signals are marked by the red dash circles. d,e) Schematic structures of the respective Ni-free LMCO and Co-free LMNO with the selected lattice oxygen highlighted by circles and arrows. f) Evolution of the selected O coordination configurations with the formation energy (ΔE) of the O vacancy. g) Schematic diagram of the density of state of TM and O.

are two different O coordination configurations considering serious Li/Ni mixing: Mn₂Li-O-NiLi₂ and Mn₂Ni-O-NiLi₂ (middle and bottom panels in Figure 5f). When charged to high potentials, Li ions around the center O atom are assumed to be completely removed. Then Mn₂Co-O-Li₃, Mn₂Li-O-NiLi₂, and Mn₂Ni-O-NiLi₂ turn into Mn₂Co-O, Mn₂-O-Ni, and Mn₂Ni-O-Ni, respectively. The formation energies of oxygen vacancy in these three configurations were then calculated to evaluate the stability of the lattice oxygen. The values are 0.76, 1.15, and 2.38 eV, respectively. It clearly demonstrates that Ni substitution can improve the stability of the oxygen anions, and the unique Li/Ni mixing in LMNO can further do a double reinforcement on the stability of the anionic framework. These results are consistent with previous reports about the density of state (DOS) analysis for TM and O (Figure 5g).[10,33] Namely, the t_{2g} state of Co^{3+}/Co^{4+} overlaps with the 2p state of O^{2-} , while the t_{2g} states of Ni²⁺/Ni³⁺/Ni⁴⁺ are far away. Therefore, these results have explicitly elucidated the impacts of Co and Ni on the oxygen stability in Mn-rich layered oxides, and especially highlighted the significance of Li/Ni mixing on stabilizing the layered framework.

2.5. Mechanism for Electrochemical Degradation

On account of the above experimental results, the roles of Co and Ni in the structure and electrochemical performance of Mn-rich

layered cathodes are summarized and schematically illustrated in Figure 6. As for Co, although it can facilitate the Li⁺ diffusion and thus deliver the highest initial capacity by increasing the interlayer spacing of Mn-rich layered oxides, more disadvantages were observed (Figure 6a). 1) It leads to severe lattice mismatch derived from the phase segregation at high potentials, which induces intragrain stress and microcracks, and finally destroys the structural integrity. 2) It results in the unstable lattice oxygen at high potentials. On the one hand, the unstable oxygen anions are easy to lose in form of O2 leading to safety issues and leaving lots of oxygen vacancies, which further induce severe TM migration and the irreversible phase transition from the layered to the spinel-like phase. On the other hand, the surficial active oxygen anions would aggravate the surficial side reactions and accelerate the surface structural degradation. All these structural negatives are thus responsible for the severe capacity and voltage degradation during the long-term cycling. Overall, Co is rather unfavorable for the structural and cycling stability of the Mnrich layered oxides. Therefore, reducing or even eliminating the Co content is plausible from the viewpoints of electrochemical performance improvement and cost cutting.

By contrast, although Ni substitution slightly reduces the cathode capacity due to the smaller interlayer spacing and serious Li/Ni mixing, it brings more advantages on the structural and electrochemical stability (Figure 6b). 1) It induces a continuous structure evolution without phase segregation

16146840, 2021, 41, Downloaded from https://advanced.onlinelibrary.wiley.com/doi/10.1002/aemn.202102646 by University Town Of Sterezhen, Wiley Online Library on [24/11/2025]. See the Terms and Conditions (https://onlinelibrary.wiley.com/term/

on Wiley Online Library for rules of use; OA articles are governed by the applicable Creative Commons

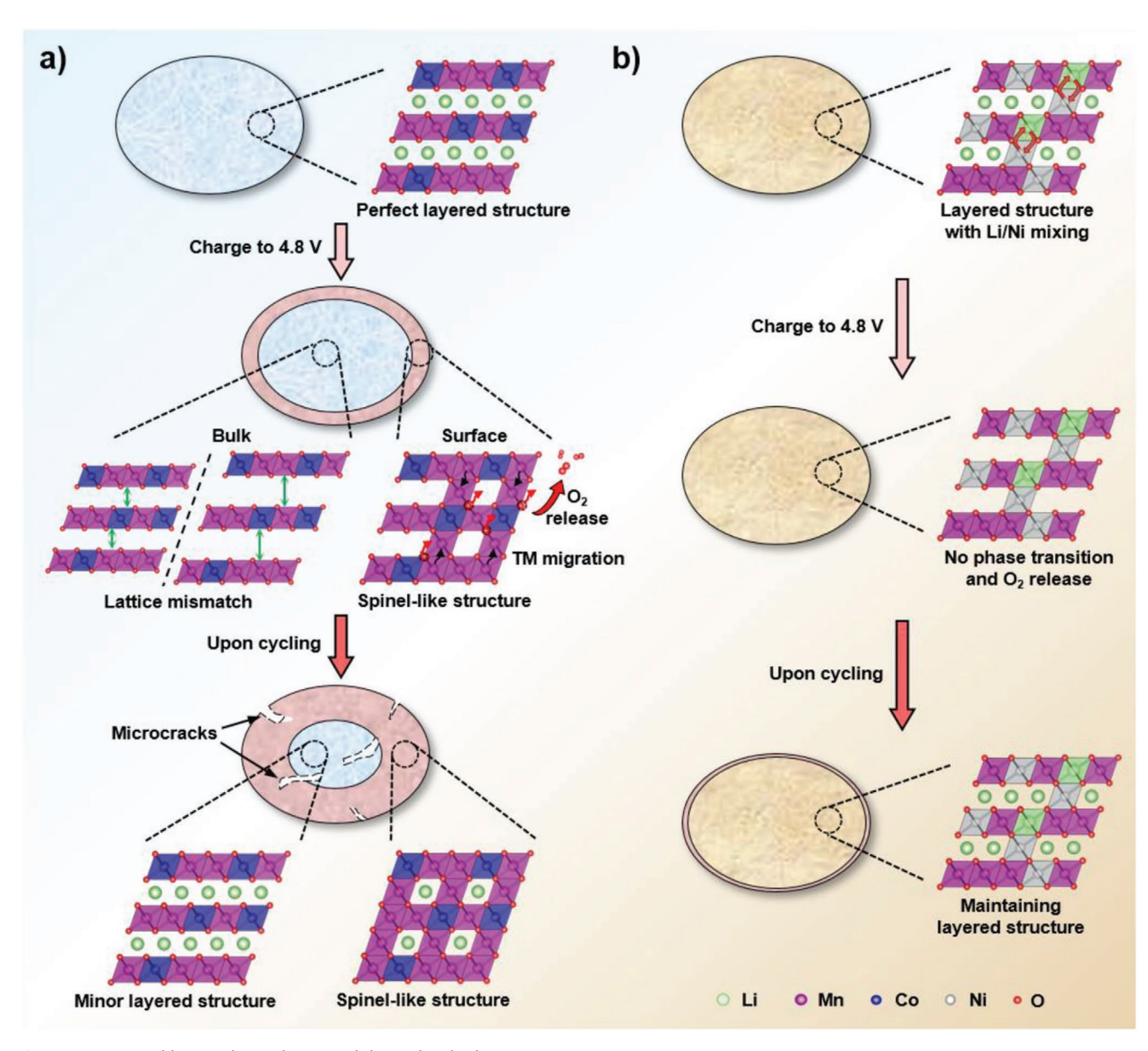


Figure 6. a) Co and b) Ni roles in the Mn-rich layered cathodes.

during charge/discharge, which thus minimizes the strain accumulation and maintains the mechanical integrity of the primary grains. 2) It greatly improves the stability of lattice oxygen at high potentials by ample Li/Ni mixing, thus suppressing the O loss, TM migration, and the adverse phase separation, and finally contributes to the superior capacity and voltage retention upon cycling. Hence, the Co-free Ni-substituted strategy is of much validity to achieve the stable Mn-rich cathode materials.

3. Conclusion

In summary, three comparable materials are investigated to understand the roles of Co and Ni in the Mn-rich layered cathodes with a high Mn content of 0.78, including the Co-substituted

LMCO, Co- and Ni co-substituted LMCNO, and the Ni-substituted LMNO. Our findings indicate that Co is destructive for the stability regarding the lattice oxygen and the structure, especially at high potentials, while the Co-free LMNO possesses excellent cyclic stability with the best capacity retention and the lowest voltage decay after the long-term cycles upon high voltages. And from various characterizations and calculations, it can be clearly claimed that the Ni substitution of Co in the Mn-rich layered cathodes can introduce more Li/Ni mixing, which greatly improves the lattice oxygen stability, the overall structural stability, and further the electrochemical performances. This work not only provides the fundamental understandings of the Co and Ni impacts on the Mn-rich cathodes, but only benefits designing the high-performance, low-cost cathode materials for the next-generation rechargeable LIBs.

ENERGY

www.advancedsciencenews.com www.advenergymat.de

4. Experimental Section

Material Synthesis Method: The traditional high-temperature solidstate reaction is known to fail to directly synthesize the stoichiometric Mn-rich layered oxides due to the thermodynamical instability nature of the layered structure. [61] The ion exchange method can obtain a material that is isostructural to the parent phase but with a new chemical composition, thus it is commonly used to prepare the Mn-rich layered oxides. [62] Therefore, it was adopted here for the synthesis of the layered LMCO, LMCNO, and LMNO.

Synthesis of Na-Containing Precursors: The carbonate ingredients $Mn_{0.78}Co_{0.22}CO_3$, $Mn_{0.78}Co_{0.11}Ni_{0.11}CO_3$, and $Mn_{0.78}Ni_{0.22}CO_3$ were first prepared by the co-precipitation method using appropriate amounts of Na_2CO_3 , $Mn(NO_3)_2\cdot 4H_2O$, $Ni(NO_3)_2\cdot 6H_2O$, and $Co(NO_3)_2\cdot 6H_2O$. The precursors of $Na_{0.7}Mn_{0.78}Co_{0.22}O_2$ (NMCO), $Na_{0.7}Mn_{0.78}Co_{0.11}Ni_{0.11}O_2$ (NMCNO), and Na_{0.7}Mn_{0.78}Ni_{0.22}O₂ (NMNO) were then synthesized via the solid-state calcination of the above sediments with an appropriate amount of Na₂CO₃ at 700 °C for 12 h.

Synthesis of Li-Containing Layered Oxides: The sodium layered precursors were thoroughly ground with the molten salt of LiNO₃/LiCl in the weight ratio of 88:12 and heated at 280 °C for 12 h to complete the Li⁺/Na⁺ ion exchange (Figure 2g). The resultants were washed with deionized water several times and dried at 120 °C in vacuum to obtain the final Mn-rich layered oxides.

Material Characterizations: The elemental composition was determined by the ICP-OES (JY2000-2, Horiba Jobin Yvon). The XRD was conducted on a Bruker D8 Advance diffractometer with a Cu Klpha radiation source, and the Rietveld refinements were performed to investigate the structures of the cathode materials. XPS with different etch depths was collected by an ESCALab220I-XL spectrometer to investigate the surface chemistry. The thermal stability was examined with a differential scanning calorimeter (Mettler Toledo) from 25 to 300 °C at a heating rate of 10 °C min⁻¹ under N₂ flow. The morphology was observed by a ZEISS Supra 55 scanning electron microscope. The microstructure and elemental distribution were, respectively, characterized by a high-resolution transmission electron microscope (JEM-100F) under 200 kV and an energy-dispersive spectrometer (Oxford X-Max 20) in the scanning-transmission mode. The aberration-corrected high-angle annular dark-field scanning transmission electron microscopy (HAADF-STEM) was performed using an FEI Titan Themis G2 double-aberration-corrected TEM at 300 kV.

Electrochemical Measurements: The electrochemical performance of the cathode materials was measured using the CR2032-type half cells. Active materials, carbon black, and PVDF binder were mixed with a weight ratio of 8:1:1 and stirred in the N-methyl-2-pyrrolidone (NMP) solvent to form the slurry, which was then cast onto aluminum foils and dried at 120 °C overnight in vacuum to obtain the cathode electrodes. The coin cells were then assembled in an argon-filled glove box together with lithium foils as the anode electrodes, Celgard films as the separators, and 1 M LiPF₆ mixing solvent in ethylene carbonate/ dimethyl carbonate/ethyl methyl carbonate with the volume ratio of 1:1:1 as the electrolyte. The charge/discharge performance was evaluated on a NEWARE battery test system. The homemade DEMS was used to monitor the in situ O₂ and CO₂ gas evolution upon cycling. The EIS was carried out on a Solartron Analylical 1470E electrochemical workstation in the frequency range from 10⁵ to 0.1 Hz.

Supporting Information

Supporting Information is available from the Wiley Online Library or from the author.

Acknowledgements

W.H. and C.L. contributed equally to this work. The authors acknowledge support from the National Key R&D Program of China (Program No. 2016YFB0700600), the Shenzhen Science and Technology Research Grant (Grant No. JCYJ20200109140416788), the Chemistry and Chemical Engineering Guangdong Laboratory (Grant No.1922018), and the National Key R&D Program of China (Program No. 2020YFB0704500).

Conflict of Interest

The authors declare no conflict of interest.

Data Availability Statement

The data that support the findings of this study are available from the corresponding author upon reasonable request.

Keywords

electrochemical performances, elementary substitution effects, Li-ion batteries, Mn-rich layered cathodes, structural chemistry

> Received: August 27, 2021 Published online: October 1, 2021

16146484, 2021, 41, Dwnholaded from https://a/wnneed.onlinelibrary.wiely.com/oi/0101002/aem.20/2102646 by University Town Of Shenzhen, Wiley Online Library on [24111025]. See the Terms and Conditions (https://onlinelibrary.wiely.com/terms-and-conditions) on Wiley Online Library for rules of use; OA articles are governed by the applicable Creative Commons

- [1] A. Kwade, W. Haselrieder, R. Leithoff, A. Modlinger, F. Dietrich, K. Droeder, Nat. Energy 2018, 3, 290.
- [2] W. Li, E. M. Erickson, A. Manthiram, Nat. Energy 2020, 5, 26.
- [3] Q. Liu, X. Su, D. Lei, Y. Qin, J. Wen, F. Guo, Y. A. Wu, Y. Rong, R. Kou, X. Xiao, F. Aguesse, J. Bareño, Y. Ren, W. Lu, Y. Li, Nat. Energy 2018, 3, 936.
- [4] J. Li, C. Lin, M. Weng, Y. Qiu, P. Chen, K. Yang, W. Huang, Y. Hong, J. Li, M. Zhang, C. Dong, W. Zhao, Z. Xu, X. Wang, K. Xu, J. Sun, F. Pan, Nat. Nanotechnol. 2021, 16, 599.
- [5] Y. Bi, J. Tao, Y. Wu, L. Li, Y. Xu, E. Hu, B. Wu, J. Hu, C. Wang, J.-G. Zhang, Y. Qi, J. Xiao, Science 2020, 370, 1313.
- [6] M. Yoon, Y. Dong, J. Hwang, J. Sung, H. Cha, K. Ahn, Y. Huang, S. J. Kang, J. Li, J. Cho, Nat. Energy 2021, 6, 362.
- [7] G. W. Nam, N.-Y. Park, K.-J. Park, J. Yang, J. Liu, C. S. Yoon, Y.-K. Sun, ACS Energy Lett. 2019, 4, 2995.
- [8] H.-H. Ryu, N.-Y. Park, J. H. Seo, Y.-S. Yu, M. Sharma, R. Mücke, P. Kaghazchi, C. S. Yoon, Y.-K. Sun, Mater. Today 2020, 36, 73.
- [9] H.-H. Ryu, G.-T. Park, C. S. Yoon, Y.-K. Sun, J. Mater. Chem. A 2019,
- 7, 18580. [10] Y. Kim, W. M. Seong, A. Manthiram, Energy Storage Mater. 2021,
- 34, 250.
- [11] N. Voronina, Y.-K. Sun, S.-T. Myung, ACS Energy Lett. 2020, 5,
- [12] M. Li, J. Lu, Science 2020, 367, 979.
- [13] L. Mu, Z. Yang, L. Tao, C. K. Waters, Z. Xu, L. Li, S. Sainio, Y. Du, H. L. Xin, D. Nordlund, F. Lin, J. Mater. Chem. A 2020, 8, 17487.
- [14] J. U. Choi, N. Voronina, Y.-K. Sun, S.-T. Myung, Adv. Energy Mater. 2020, 10, 2002027.
- [15] H. Li, M. Cormier, N. Zhang, J. Inglis, J. Li, J. R. Dahn, J. Electrochem. Soc. 2019, 166, A429.
- [16] N. Nitta, F. Wu, J. T. Lee, G. Yushin, Mater. Today 2015, 8, 252.
- [17] T. Liu, A. Dai, J. Lu, Y. Yuan, Y. Xiao, L. Yu, M. Li, J. Gim, L. Ma, J. Liu, C. Zhan, L. Li, J. Zheng, Y. Ren, T. Wu, R. Shahbazian-Yassar, J. Wen, F. Pan, K. Amine, Nat. Commun. 2019, 10, 4721.
- [18] W. Huang, G. Wang, C. Luo, Y. Xu, Y. Xu, B. J. Eckstein, Y. Chen, B. Wang, J. Huang, Y. Kang, J. Wu, V. P. Dravid, A. Facchetti, T. J. Marks, Nano Energy 2019, 64, 103936.



www.advenergymat.de

ENERG

16146840, 2021, 41, Downloaded from https://advanced.onlinelibrary.

wiley.com/doi/10.1002/aenm.202102646 by University Town Of Shenzhen, Wiley Online Library on [24/11/2025]. See the Terms

and Conditions (https://onlinelibrary.wiley

on Wiley Online Library

for rules of use; OA

by the applicable Creative Commons

- [19] A. Manthiram, K. Chemelewski, E.-S. Lee, Energy Environ. Sci. 2014, 7, 1339.
- [20] M. Kuenzel, G.-T. Kim, M. Zarrabeitia, S. D. Lin, A. R. Schuer, D. Geiger, U. Kaiser, D. Bresser, S. Passerini, *Mater. Today* 2020, 39, 127.
- [21] A. R. Armstrong, P. G. Bruce, Nature 1996, 381, 499.
- [22] X. Zhu, F. Meng, Q. Zhang, L. Xue, H. Zhu, S. Lan, Q. Liu, J. Zhao, Y. Zhuang, Q. Guo, B. Liu, L. Gu, X. Lu, Y. Ren, H. Xia, Nat. Sustainability 2021, 4, 392.
- [23] J. K. Papp, N. Li, L. A. Kaufman, A. J. Naylor, R. Younesi, W. Tong, B. D. McCloskey, *Electrochim. Acta* 2021, 368, 137505.
- [24] J. Rana, M. Stan, R. Kloepsch, J. Li, G. Schumacher, E. Welter, I. Zizak, J. Banhart, M. Winter, Adv. Energy Mater. 2014, 4, 1300998.
- [25] P. Yan, L. Xiao, J. ZHeng, Y. Zhou, Y. He, X. Zu, S. X. Mao, J. Xiao, F. Gao, J.-G. Zhang, C.-M. Wang, Chem. Mater. 2015, 27, 975.
- [26] M. Gu, I. Belharouak, J. Zheng, H. Wu, J. Xiao, A. Genc, K. Amine, S. Thevuthasan, D. R. Baer, J.-G. Zhang, N. D. Browning, J. Liu, C. Wang, ACS Nano 2013, 7, 760.
- [27] M. Tian, Y. Gao, Z. Wang, L. Chen, Phys. Chem. Chem. Phys. 2016, 18, 17345.
- [28] J. M. Paulsen, J. R. Dahn, Solid State Ionics 1999, 126, 3.
- [29] T. Sato, K. Sato, W. Zhao, Y. Kajiya, N. Yabuuchi, J. Mater. Chem. A 2018. 6, 13943.
- [30] Z. Lu, R. A. Donaberger, J. R. Dahn, Chem. Mater. 2000, 12, 3583.
- [31] X. Wang, X. Yang, H. Zheng, T. Shen, Z. Zhang, Solid State Ionics 2005, 176, 1043.
- [32] J. Kim, H. Lee, H. Cha, M. Yoon, M. Park, J. Cho, Adv. Energy Mater. 2018, 8, 1702028.
- [33] M. S. Whittingham, Chem. Rev. 2004, 104, 4271.
- [34] J. Xu, F. Lin, M. M. Doeff, W. Tong, J. Mater. Chem. A 2017, 5, 874.
- [35] P. hou, H. Zhang, Z. Zi, L. Zhang, X. Xu, J. Mater. Chem. A 2017, 5, 4254.
- [36] K. Min, K. Park, S. Y. park, S.-W. Seo, B. Choi, E. Cho, J. Electrochem. Soc. 2018, 165, A79.
- [37] E. Rossen, C. D. W. Jones, J. R. Dahn, Solid State Ionics 1992, 57, 311.
- [38] M. E. Spahr, P. Novák, B. Schnyder, O. Haas, R. Nesper, J. Electrochem. Soc. 1998, 145, 1113.
- [39] J. Zheng, S. Myeong, W. Cho, P. Yan, J. Xiao, C. Wang, J. Cho, J.-G. Zhang, Adv. Energy Mater. 2017, 7, 1601284.
- [40] P. K. Nayak, E. M. Erickson, F. Schipper, T. R. Penki, N. Munichandraiah, P. Adelhelm, H. Sclar, F. Amalraj, B. Markovsky, D. Aurbach, Adv. Energy Mater. 2018, 8, 1702397.
- [41] Y. Lyu, X. Wu, K. Wang, Z. Feng, T. Cheng, Y. Liu, M. Wang, R. Chen, L. Xu, J. Zhou, Y. Lu, B. Guo, Adv. Energy Mater. 2021, 11, 2000982.
- [42] L. Wang, B. Chen, J. Ma, G. Cui, L. Chen, Chem. Soc. Rev. 2018, 47, 6505.

- [43] J. Liang, D. Wu, M. Hu, Y. Tian, J. Wei, Z. Zhou, Electrochim. Acta 2014, 146, 784.
- [44] A. W. Moses, H. G. G. Flores, J.-G. Kim, M. A. Langell, Appl. Surf. Sci. 2007, 253, 4782.
- [45] Y. Xiao, T. Liu, J. Liu, L. He, J. Chen, J. Zhang, P. Luo, H. Lu, R. Wang, W. Zhu, Z. Hu, G. Teng, C. Xin, J. Zheng, T. Liang, F. Wang, Y. Chen, Q. Huang, F. Pan, H. Chen, Nano Energy 2018, 49, 77.
- [46] J. Zheng, G. Teng, C. Xin, Z. Zhuo, J. Liu, Q. Li, Z. Hu, M. Xu, S. Yan, W. Yang, F. Pan, J. Phys. Chem. Lett. 2017, 8, 5537.
- [47] T. Liu, L. Yu, J. Liu, J. Lu, X. Bi, A. Dai, M. Li, M. Li, Z. Hu, L. Ma, D. Luo, J. Zheng, T. Wu, Y. Ren, J. Wen, F. Pan, K. Amine, Nat. Energy 2021, 6, 277.
- [48] K. Kang, Y. S. Meng, J. Bréger, C. P. Grey, G. Ceder, Science 2006, 311 977
- [49] H. Yu, Y. Qian, M. Otani, D. Tang, S. Guo, Y. Zhu, H. Zhou, Energy Environ. Sci. 2014, 7, 1068.
- [50] H.-J. Noh, S. Youn, C. S. Yoon, Y.-K. Sun, J. Power Sources 2013, 233, 121.
- [51] J. Zheng, Y. Ye, T. Liu, Y. Xlao, C. Wang, F. Wang, F. Pan, Acc. Chem. Res. 2019, 52, 2201.
- [52] H. Pan, S. Zhang, J. Chen, M. Gao, Y. Liu, T. Zhu, Y. Jiang, Mol. Syst. Des. Eng. 2018, 3, 748.
- [53] Y. Li, Z. Li, C. Chen, K. Yang, B. Cao, S. Xu, N. Yang, W. Zhao, H. Chen, M. Zhang, F. Pan, J. Energy Chem. 2021, 61, 368.
- [54] D. Wang, C. Xin, M. Zhang, J. Bai, J. Zheng, R. Kou, J. Y. P. Ko, A. Huq, G. Zhong, C.-S. Sun, Y. Yang, Z. Chen, Y. Xlao, K. Amine, F. Pan, F. Wang, Chem. Mater. 2019, 31, 2731.
- [55] W. Liu, P. Oh, X. Liu, M.-J. Lee, W. Cho, S. Chae, Y. Kim, J. Cho, Angew. Chem., Int. Ed. 2015, 54, 4440.
- [56] D. Wang, R. Kou, Y. Ren, C.-J. Sun, H. Zhao, M.-J. Zhang, Y. Li, A. Huq, J. Y. P. Ko, F. Pan, Y.-K. Sun, Y. Yang, K. Amine, J. Bai, Z. Chen, F. Wang, Adv. Mater. 2017, 29, 1606715.
- [57] X. R. Yang, M. Lin, G. R. Zheng, J. Wu, X. S. Wang, F. C. Ren, W. G. Zhang, Y. Liao, W. M. Zhao, Z. R. Zhang, N. B. Xu, W. L. Yang, Y. Yang, Adv. Funct. Mater. 2020, 30, 2004664.
- [58] D. Ensling, G. Cherkashinin, S. Schmid, S. Bhuvaneswari, A. Thissen, W. Jaegermann, Chem. Mater. 2014, 26, 3948.
- [59] J. A. Gilbert, J. Bareño, T. Spila, S. E. Trask, D. J. Miller, B. J. Polzin, A. N. Jansen, D. P. Abraham, J. Electrochem. Soc. 2016, 164, A6054.
- [60] W. Li, X. Liu, H. Celio, P. Smith, A. Dolocan, M. Chi, A. Manthiram, Adv. Energy Mater. 2018, 8, 1703154.
- [61] F. Capitaine, P. Gravereau, C. Delmas, Solid State Ionics 1996, 89, 197.
- [62] H. Gwon, S.-W. Kim, Y. U. Park, J. Hong, G. Ceder, S. Jeon, K. Kang, Inorg. Chem. 2014, 53, 8083.